Computational Materials Science 228 (2023) 112369

Contents lists available at ScienceDirect

Computational Materials Science

journal homepage: www.elsevier.com/locate/commatsci

Full length article

Effect of periodic image interactions on kink pair activation of screw dislocation

Fei Shuang [a,f], Rigelesaiyin Ji [d,g], Liming Xiong [d,e], Wei Gao [a,b,c,*]

[a] Department of Mechanical Engineering, The University of Texas at San Antonio, San Antonio, TX 78249, United States
[b] J. Mike Walker'66 Department of Mechanical Engineering, Texas A&M University, College Station, TX 77843, United States
[c] Department of Materials Science & Engineering, Texas A&M University, College Station, TX 77843, United States
[d] Department of Aerospace Engineering, Iowa State University, Ames, IA 50011, United States
[e] Department of Mechanical and Aerospace Engineering, North Carolina State University, Raleigh, NC, 27695, United States
[f] Department of Materials Science and Engineering, Faculty of Mechanical, Maritime and Materials Engineering, Delft University of Technology, Mekelweg 2, 2628CD, Delft, The Netherlands
[g] 3MT Modeling and Simulation Group, Schlumberger, Sugar Land, TX

ARTICLE INFO

Keywords:
Kink pair
Screw dislocation
Activation barrier
Periodic image interactions
Nudged elastic band

ABSTRACT

Periodic boundary condition along a dislocation line is commonly used in computing activation barriers or formation energies of kink pair of screw dislocation in BCC metals. Although the effect of periodic image interactions on the computation results is obvious, there had been no comprehensive analysis on such effect. In this work, we quantify it through combined nudged elastic band (NEB) simulations and theoretical analysis based on dislocation mechanics. The NEB calculation result demonstrates a non-negligible size dependence on the activation barrier at zero and low stresses. The theoretical analysis offers a practical approach to quantify such size effect without the need of time-consuming NEB simulations. Notably, a simple relationship between kink activation barrier and dislocation line length is derived at zero stress, offering a new approach to compute kink pair formation energy based on NEB simulation results.

1. Introduction

Screw dislocation motion through kink pair activation determines the mechanical strength and ductility of BCC metals [1]. As such, it is important to understand the mechanism of this motion and quantify the key parameters such as kink activation barrier [2], formation energy [3] and diffusion coefficient [4]. Extensive atomistic computation efforts have been dedicated to the thermodynamics and kinetics of kink pair at different time scales. For example, molecular statics has been used to compute the Peierls stress at different crystal orientations [5,6]. Molecular dynamics has also been performed to examine the motion of screw dislocations at finite temperatures [5,7–9], which however occurred in a very short time scale under an unrealistic high stress. Alternatively, the Nudged Elastic Band (NEB) method has been applied to study the activation of screw dislocations. The activation energy barrier H_b obtained from NEB can be used to estimate the kink pair activation rate based on harmonic transition state theory, which can be further applied to inform experiments and higher scale simulations. For example, previous NEB calculations [10] were carried out to capture the single-humped minimum energy path (MEP) with an embedded atom method (EAM) potential named MCM2011 [11]. In this study, the nucleation, propagation and annihilation of the kink pair and the activation barriers under different stresses were studied and the resulting parameters were used to inform the crystal plasticity model. It should be noted that the kink activation barrier obtained from NEB is purely enthalphic, and the entropic contribution to the activation rate is absorbed by the pre-factor in the rate equation. Alternatively, the entropic contribution to the kink pair activation can be obtained from free energy sampling. For example, a recent study computed the Gibbs free energy barrier of kink pair activation in BCC Nb from MD and hyperdynamics simulations, and then estimated the contribution of entropy with an empirical fitting function [12]. In addition to empirical interatomic potentials, a machine learning potential trained by Gaussian process regression was used to study the screw dislocation structure and mobility in BCC Fe. The results indicated that the Gaussian Approximation Potential (GAP) predicts more reliable core structure and Peierls potential than previous EAM potentials [13]. On the other side, DFT has been also applied to compute kink pair activation barrier as a function of stress in BCC metals using a line tension model [14]. The comparison between interatomic potentials,

* Correspondence to: J. Mike Walker'66 Department of Mechanical Engineering, Texas A&M University, 77843, College Station, United States.
E-mail address: wei.gao@tamu.edu (W. Gao).

https://doi.org/10.1016/j.commatsci.2023.112369
Received 13 February 2023; Received in revised form 2 July 2023; Accepted 4 July 2023
Available online 15 July 2023

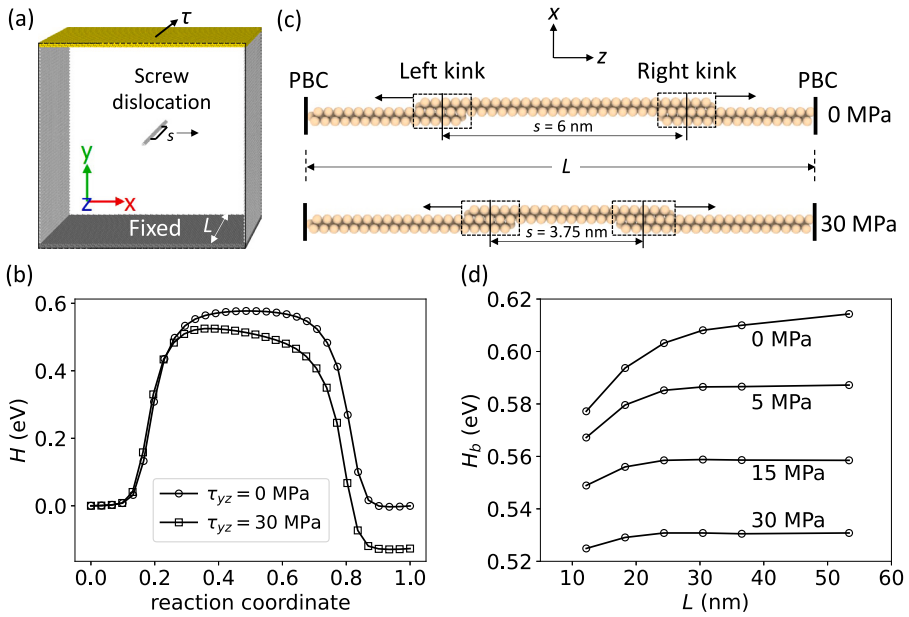

Fig. 1. (a) NEB simulation set-up. (b) Saddle configurations of kink pair activation. Only defect atoms are shown. (c) The minimum energy paths when τ = 0 and 30 MPa. (d) Length-dependent kink pair activation enthalpy barriers under different stress levels.

DFT and experiments on kink pair activation can be found in a recent review paper [15].

Notably, recent computational studies on BCC Fe and W demonstrates an interesting simulation cell size-dependent kink mobility due to image stress induced by the periodic boundary conditions imposed on the simulation cell [16,17], raising a question of how the kink pair activation depend on the simulation cell size along dislocation line. Although the effect of image interactions on kink pair activation was discussed in previous studies [18,19], a thorough and quantitative analysis on such effect has been missing. In this paper, NEB simulations and theoretical analysis based on dislocation mechanics are combined to quantify the size effect on the kink pair activation barrier.

2. Nudged elastic band simulation

The atomistic configuration employed in our NEB calculations is shown in Fig. 1(a). The x, y and z axes are oriented along the [111], [$\bar{1}$01] and [$\bar{1}2\bar{1}$] directions, respectively. The dimensions along the x and y directions are 25 nm, and the dimension along the z direction is varied from 12 nm to 54 nm to examine how the periodic images affect the kink pair activation. The periodic boundary condition is adopted in the z direction, while free boundary conditions are used in the x and y directions. The initial configuration of a 1/2[111] screw dislocation is introduced at the center of the supercell by superimposing its elastic displacement [20], as shown in Fig. 1(a). All simulations are conducted using the LAMMPS [21]. The climbed image NEB method [22] is performed to determine the MEP of screw dislocation migration. The final configuration of the screw dislocation after migration is created by the same procedure as the initial configuration but the dislocation is shifted to the adjacent {110} Peierls valley. The intermediate images in NEB calculation are specifically generated by introducing a kink pair along the screw dislocation line with a linearly varied distance, which is used to avoid the formation of multiple stack-on kink pairs in MEP search and accelerate the convergence of NEB calculations. At least 16 NEB images are used to guarantee accuracy in all calculations. All NEB calculations are considered to be converged when the maximum force of atoms is below 0.01 eV/Å. To study the effect of shear stress on MEP, the NEB calculations are performed under different shear stresses (τ). It is noted that stress-controlled NEB calculation can be done using solid-state NEB methods such as G-SSNEB [23], which was recently improved to get more accurate MEP and barrier under finite deformation [24]. Since the solid-state NEB methods have not been implemented in LAMMPS, we use an alternative and approximate approach to apply shear stress as introduced in [13]. In this approach, equivalent forces are applied to the atoms on the top boundary of the system along negative z direction, while the atoms on the bottom boundary are fixed. Both boundaries contain three layers of atoms. In this way, the screw dislocation can be approximately considered under a constant stress since it is far away from the boundaries where the external force is applied. The simulation results are visualized by the software OVITO [25].

BCC Fe is used as a model material in our study and EAM potential [11] is used to describe the atomistic interactions. Fig. 1(b–d) show the NEB results. The MEPs are plotted in Fig. 1(b) for L = 12 nm when τ = 0 and 30 MPa. The single-humped MEP shape is consistent with previous study [10]. When τ = 0, the MEP is a symmetric shape, since the initial and final states are equivalent in the current simulation setup and the free boundary effect is negligible. The applied shear stress promotes the migration of screw dislocation, therefore yielding a lower barrier compared with zero stress case. Fig. 1(c) shows the saddle configurations. The nucleated kink pair first separates into two individual kinks (the left and right ones), which then propagate towards opposite directions along the dislocation line. Note that there is an attractive force between those two kinks, similar to the attractive force between two electrical charges of opposite sign [26]. It is the spring force in NEB and the applied shear stress drive these two kinks to move away from each other after separation. In zero stress case, the distance between two individual kinks at the saddle equals half of the dislocation length $L/2$ = 6 nm. When shear stress is applied, the saddle moves closer to the initial state, leading to a smaller distance between the kinks at the saddle.

The NEB calculations are conducted for different values of L at several stress levels. The calculated barriers, plotted in Fig. 1(d), display the size dependence due to the effect of periodic image interactions, although such size effect is depressed by the applied shear stress. The variation of barriers can be intuitively explained as follow. Two separated kinks shown in Fig. 1(c) are both attracted by the kinks in the closest periodic images. Such attraction facilitates the kink separation and migration of the screw dislocation. Therefore, it lowers the barrier when the dimension of the simulation cell along the dislocation line

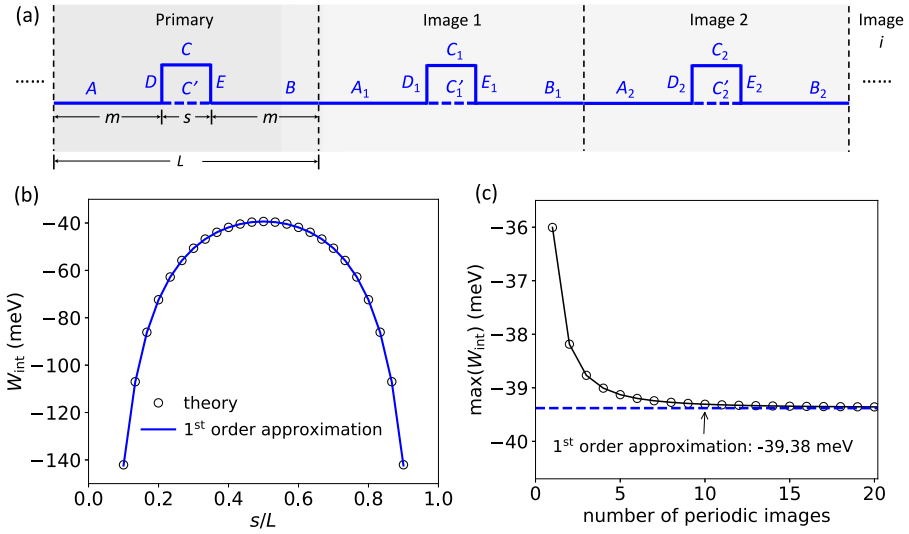

Fig. 2. (a) Schematic of periodic kink pairs. (b) Interaction energy calculated by including 20 periodic images, compared with first order approximation. (c) Convergence of the maximum interaction energy.

direction decreases. On the other side, when the cell length goes to infinity, the distance between the kinks also goes to infinity. Then, the barrier should approach to the energy corresponding to the formation of two non-interacting single kinks. This kink formation energy can be computed using atomistic simulations [3]. It is shown from our NEB results that the relative difference in barriers between the smallest model and the largest one is around 6.4%, which may result in unwanted error if the barriers computed from nanoscale simulations are applied to the applications in which the length of dislocation is much longer. Next, we present a theoretical analysis to quantify the effects of periodic image interactions on kink pair activation on a screw dislocation line.

3. Dislocation mechanics analysis

The schematic of a periodic kink pair array for the analytical analysis is shown in Fig. 2(a), where the kinked dislocation line is divided into multiple horizontal and vertical segments. The change of enthalpy due to the kink pair formation can be expressed as [26]:

$$H(s, L) = E_0 + W_{\text{int}}(s, L) - \tau bhs, \tag{1}$$

where E_0 is the formation energy of the two kinks (segments D and E in Fig. 2(a)), W_{int} is the interaction energy between the dislocation segments, and τbhs denotes the work done by the applied shear stress (where τ is the shear stress, b the magnitude of Burgers vector, h the kink height and s the separation distance between two single kinks). For a given material and applied stress, b, h and τ are fixed, so the enthalpy is only a function of s and L. The formation energy E_0 only depends on the kink height h, so the only term that controls the cell size dependence is the interaction energy W_{int}. As shown in our NEB calculations, the enthalpy displays a single-humped shape as a function of s. Therefore, the enthalpy barrier H_b can be obtained by maximizing H with respect to s, i.e.,

$$H_b = E_0 + \max\left(W_{\text{int}} - \tau bhs\right). \tag{2}$$

Since E_0 is the intrinsic property of the kink pair which is independent of simulation box size, we can define the change of enthalpy barrier as:

$$\Delta H_b(\tau, L) = E_b - E_0 = \max\left(W_{\text{int}} - \tau bhs\right). \tag{3}$$

Next, we formulate the interaction energy W_{int} between dislocation segments. W_{int} is composed of two parts: the interaction energy between the dislocations A, B, C, D, E and C' in the primary image (shown in Fig. 2(a)), and the interaction energy between those primary dislocations and the dislocations in the periodic images A_i, B_i, C_i, D_i and C_i'. These two parts of interaction are respectively represented by W^0 and W^i_{image} (i is the periodic image index), i.e.

$$W_{\text{int}} = W^0 + \sum_{i=1}^{\infty} W^i_{\text{image}}. \tag{4}$$

Further, the interaction energy can be separated into the contributions from the vertical and horizontal dislocation segments:

$$W^0 = W^0_{\text{v}} + W^0_{\text{h}}, \tag{5}$$

and

$$W^i_{\text{image}} = W^i_{\text{v}} + W^i_{\text{h}}. \tag{6}$$

Eqs. (5) and (6) can be written in terms of the summation of interaction energies between parallel dislocation pairs since interaction vanishes for orthogonal segments, therefore

$$W^0_{\text{v}} = W_{\text{v}}(D, E), \tag{7}$$

$$W^0_{\text{h}} = \left[W_{\text{h}}(A, C) - W_{\text{h}}\left(A, C'\right) + W_{\text{h}}(B, C) - W_{\text{h}}\left(B, C'\right)\right], \tag{8}$$

$$W^i_{\text{v}} = W_{\text{v}}\left(D, D_i\right) + W_{\text{v}}\left(D, E_i\right) + W_{\text{v}}\left(E, D_i\right) + W_{\text{v}}\left(E, E_i\right), \tag{9}$$

$$W^i_{\text{h}} = 2\left[W_{\text{h}}\left(A, C_i\right) - W_{\text{h}}\left(A, C_i'\right) + W_{\text{h}}\left(B, C_i\right) - W_{\text{h}}\left(B, C_i'\right)\right], \tag{10}$$

where Eq. (10) is simplified by the fact that some dislocation pairs are equivalent due to symmetry.

It is straightforward to derive the expressions of W_{v} and W_{h} in Eqs. (7)–(10) based on the general form of the interaction energy between two parallel dislocations segments [26]. The detailed process is presented in Appendix A. Although the final formula of W_{int} is in a lengthy form, its value can be calculated with a selected number of periodic images included in the summation of Eq. (4). Taking the first 20 periodic images, we compute W_{int} as a function of λ with L = 12 nm and the material parameters of BCC Fe (μ = 115.99 GPa, b = 2.4885 Å, h = 2.293 Å, ν = 0.29). As shown in Fig. 2(b), the result displays a single-humped shape, similar to the MEP obtained from NEB calculation. To check the effects of image number on the summation in

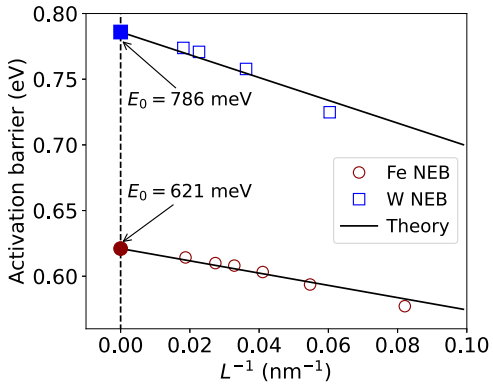

Fig. 3. Comparison between NEB and first order approximation.

Eq. (4), the peak values of W_{int} are plotted in Fig. 2(c) as a function of image number included in the summation. It is found that $\max(W_{\text{int}})$ converges rapidly and varies less than 0.002 meV when the number of the images under consideration reaches 20, although the previous study claimed a long-range interaction between two kinks [18].

To gain more insights, we simplify the lengthy expression of W_{int} using a first-order approximation. As shown in Appendix B, the simplified formula can be derived as

$$W_{\text{int}} = -\frac{\mu b^2 h^2}{8\pi L}\frac{1+\upsilon}{1-\upsilon}\left[\frac{1}{\lambda} + \sum_{i=1}^{\infty}\left(\frac{1}{i+\lambda} + \frac{1}{i-\lambda} - \frac{2}{i}\right)\right], \tag{11}$$

where $\lambda = s/L$ and the summation of the infinite series is convergent since

$$\frac{1}{i+\lambda} + \frac{1}{i-\lambda} - \frac{2}{i} = \mathcal{O}\left(\frac{1}{i^3}\right), \tag{12}$$

and $1/i^3$ is a rapidly converged p series. Then, we compute W_{int} with Eq. (11) using the first 20 terms of the series and the materials parameters of Fe. The result is plotted in Fig. 2(b), which shows that the first order approximation produces indistinguishable result, suggesting the first order approximation is accurate enough to compute the interaction energy. It is noted that $W_{\text{int}}(s) = W_{\text{int}}(L-s)$ in Eq. (11), so that W_{int} is symmetric about $\lambda = 1/2$, at which W_{int} reaches maximum. Although it is non-trivial to obtain the exact summation of the infinite series in Eq. (11), the summation can be numerically evaluated up to a given precision. For example, when $\lambda = 1/2$, the series summation is 0.77 to the second decimal of accuracy, so the approximation of $\max(W_{\text{int}})$ or ΔH_b when $\tau = 0$ is:

$$\Delta H_b(\tau = 0) = \max(W_{\text{int}}) \approx -2.77\frac{\mu b^2 h^2}{8\pi L}\frac{1+\upsilon}{1-\upsilon}. \tag{13}$$

Apply materials properties of BCC Fe, $\max(W_{\text{int}}) \approx -39.38$ meV. Fig. 2(c) shows that the curve obtained from direct summation converges to this value, suggesting the convergence of the summation in Eq. (4), which was not rigorously proved though. Combine Eqs. (2) and (13), the length dependent activation barrier of periodic kink pairs can be finally written as

$$H_b(\tau = 0) \approx E_0 - 2.77\frac{\mu b^2 h^2}{8\pi L}\frac{1+\upsilon}{1-\upsilon}, \tag{14}$$

When $L \to \infty$, there is no interaction between the kinks moving towards left and right at the saddle point, so the barrier equals to the formation energy of two individual kinks E_0 which is an intrinsic material property.

Next, the analytical results are compared with NEB simulations. The first order approximation shows that the barrier change is inversely proportional to the dislocation line length L. Therefore, we fit the activation barriers H_b calculated from NEB as a function of L^{-1} with Eq. (14) using least square method, where the slope of the linear fitting is fixed and the kink formation energy E_0 is taken as the fitting parameter. In addition to the results of BCC Fe, the activation barriers of BCC W are also calculated with NEB at zero shear stress. The material properties of W are $\mu = 148.02$ GPa, $b = 0.27478$ nm, $h = 0.2532$ nm, $\nu = 0.28$. The fittings, plotted in Fig. 3, are closely aligned with the NEB results. The slope of the fitting line is dependent on a material coefficient $K = \mu b^2 h^2(1+\nu)/(1-\nu)$. Since $K(\text{Fe}) < K(\text{W})$, the activation barrier of Fe converges faster than that of W, which is similar to the convergence of the diffusion coefficient of these two metals reported in [16]. From the fitting, the kink formation energies E_0 of BCC Fe and W are respectively 621 meV and 786 meV. In a previous study [3], E_0 of Fe was computed to be 650 meV by molecular statics simulation, which is greater than the fitted value. The difference may come from three sources. First, a different empirical potential was used in the previous study. Second, since periodic boundary condition was used in the previous study, the calculation was influenced by the similar effects of periodic image interactions as discussed in the present study. Although a convergence test with respect to the length of periodic box was conducted in the previous study, the convergence of E_0 did not achieve the accuracy of meV. In fact, following the convergence trend reported in that study, a slightly lower value of E_0 should be expected for large simulation boxes. Third, a sharp kink is used in our NEB and analytical model as an approximation, however a finite kink width was reported in [3]. For BCC W, the fitted formation energy 786 meV is greater than the previously reported value of 750 meV [27]. Although the reference used the same empirical potential as our study, the effect of periodic image interaction was not discussed in the reference, which may impact the result. Due to the limitation of previous calculations of formation energy, we suggest an alternative approach to obtain the formation energy using NEB calculations along with the result from first order approximation. On the other side, the first order approximation can be used to predict the activation barrier of kink pair in a large periodic box based on the NEB calculation conducted on a small periodic box. This is particularity useful when NEB calculation is computationally expensive. For example, Eq. (14) can be used to calculate the activation barrier of kink pair at the scale of micrometers for dislocation dynamics or kinetic Monte Carlo simulations. Moreover, when the formation energy E_0 is known, Eq. (14) can be applied to estimate activation barrier for a given periodic box without the need of NEB calculations.

Finally, when subjected to shear stress, the theoretical analysis explains the suppressed size effect on the barrier as observed in NEB calculations. In Fig. 4(a), the single-humped enthalpy profile computed for BCC Fe is positively skewed due to the contribution from the work done by stress. Using the same E_0 obtained above, the theoretical predictions of ΔH_b as a function of periodic simulation cell size are compared with NEB results in Fig. 4(b) and show good agreement. Apparently, the size effect is a result of competition between the size-dependent interaction energy and external work done by stress. In the case of BCC Fe, the latter term dominates even at small stresses, therefore, a suppressed size effect is shown at 5 MPa. To quantify the combined effect of shear stress and the length of a dislocation line, we introduce $\mathcal{V}(\tau, L)$ to measure the barrier variation resulting from periodic image interactions, which is defined by

$$\mathcal{V}(\tau, L) = -\Delta H_b(\tau, L) + \Delta H_b(\tau, \infty). \tag{15}$$

Since it is computationally infeasible to directly evaluate $\Delta H_b(\tau, \infty)$, we approximate this term using $L = 1000$ nm, where periodic image interactions can be disregarded. A contour plot of $\mathcal{V}(\tau, L)$ for BCC Fe is shown in Fig. 5(a), illustrating non-negligible effects of periodic image interactions even at non-zero stresses at small L values around 10 nm. Additionally, in Fig. 5(b), the contour line corresponding to $\mathcal{V} = 5$ meV is plotted for several BCC metals, showing that W exhibits the most pronounced effects of periodic image interactions, while Nb and V display the least impact.

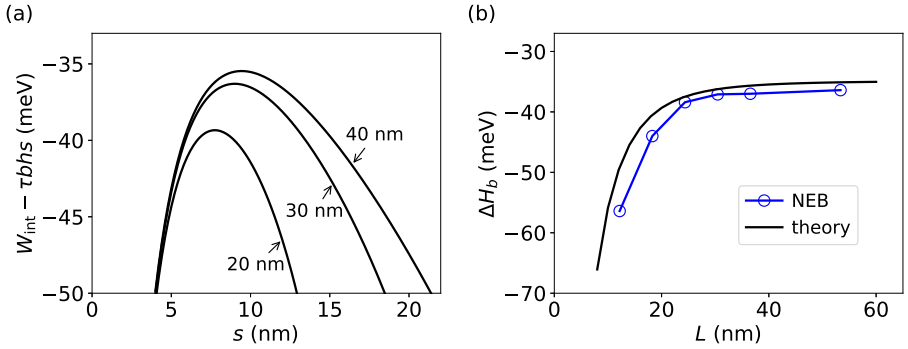

Fig. 4. (a) Theoretical results of enthalpy change for different box size when $\tau = 5$ MPa. (b) Comparison of length-dependent barrier change when $\tau = 5$ MPa.

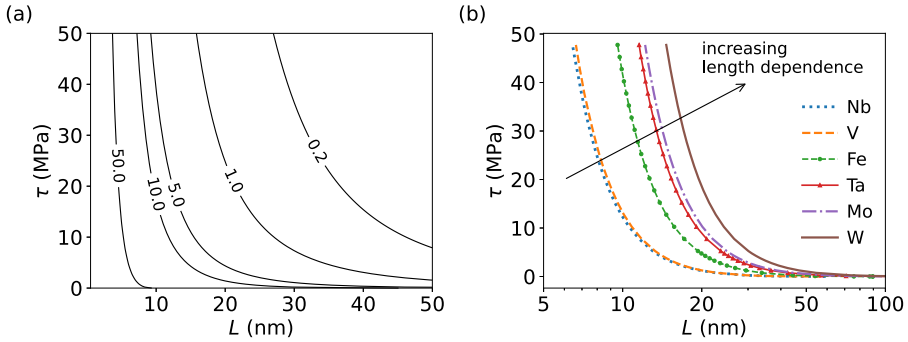

Fig. 5. (a) Contour of the barrier variation $\mathcal{V}(\tau, L)$ defined in Eq. (15) for BCC Iron (unit: meV). (b) Comparison of the contour line corresponding to 5 meV for different BCC metals.

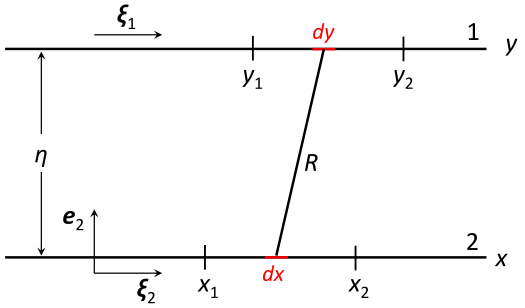

Fig. A.6. Coordinates for the interaction between two parallel dislocations 1 and 2.

4. Discussion

It is shown from our study that the size dependence on kink activation barrier is important for zero stress and low stress regime, when kink interaction energy dominates over external work done by stress. Notably, the low stress regime is unavoidable in experiments. The pioneering experiments [28–30] on characterizing the kink-controlled dislocation mobility in BCC Fe were all performed in low stress regime (less than 30 MPa). An interpretation of the results from such experiments necessitates the simulations in low stress regime.

The size dependence of the kink activation barrier becomes insignificant at high stresses, which allows for the calculation of barriers within a relatively small computational cell. As such, an alternative approach for estimating the barriers at low stresses is to directly extrapolate $H_b(\tau)$ from high stresses to zero and low stresses, using an empirical fit of the Kocks law [31]. To ensure the accuracy of this fit, it is necessary to conduct a sufficient number of barrier calculations at high stress levels. However, certain concerns may arise: At what stress level, the size effect could be confidently neglected, particularly if the material has not been thoroughly studied? What range of stresses needs to be taken into account to ensure a reasonable fit? While both approaches have their respective merits, the present study delivers a comprehensive analysis of the size dependence of activation barrier at zero and low stresses, which is not captured through fitting the overdriven simulation data into the Kocks law.

This study focuses on the impacts of periodic image interactions along a screw dislocation line, while the remaining two directions of the simulation box are considerably large and subjected to free boundary conditions, as depicted in Fig. 2. Notably, the image force resulting from the free boundary along the x-direction contributes to the activation barrier as it does work during kink pair activation. Interestingly, this work is proportional to the length of dislocation line. The competing size effects arising from the free and periodic boundaries warrants further exploration. In some studies, periodic boundary condition has also been applied along x-direction. In these cases, the size effect can be evaluated along both periodic directions employing the theoretical framework developed in this study.

5. Summary

In summary, the effect of periodic image interactions on the kink pair activation of screw dislocation in BCC metals are investigated by NEB simulations and theoretical analysis. NEB simulations show that the activation barrier of the kink pair increases with the simulation box size along the dislocation line direction. Such size effect is analyzed using a dislocation mechanics model based on the elastic interaction of

the periodic kink pairs. Under zero shear stress condition, the relationship between activation barrier and periodic box length is derived using first order approximation. The application of this work is twofold. First, the theory can be used to predict the activation barrier of kink pair in a large periodic box based on the NEB calculation conducted on a small simulation cell. Second, it is noted that the effect of periodic image interaction on kink pair formation energy was not thoroughly examined in previous atomistic simulations, so a new approach is proposed to compute kink pair formation energy using NEB calculated activation barriers.

CRediT authorship contribution statement

Fei Shuang: Methodology, Software, Investigation, Writing – original draft, Writing – review & editing. **Rigelesaiyin Ji:** Investigation, Writing – review & editing. **Liming Xiong:** Investigation, Writing – review & editing, Supervision, Funding acquisition. **Wei Gao:** Conceptualization, Methodology, Investigation, Writing – original draft, Writing – review & editing, Supervision, Funding acquisition.

Declaration of competing interest

The authors declare that they have no known competing financial interests or personal relationships that could have appeared to influence the work reported in this paper.

Data availability

Data will be made available on request

Acknowledgments

W.G. and F.S. gratefully acknowledge financial support of this work by the National Science Foundation, United States through Grant no. CMMI-2308163 and CMMI-2305529. The authors acknowledge the Texas Advanced Computing Center (TACC) at the University of Texas at Austin for providing HPC resources that have contributed to the research results reported within this paper. LX acknowledges the support from National Science Foundation, United States through CMMI-2322675 and CMMI-2328533. JR and LX acknowledge the Extreme Science and Engineering Discovery Environment (XSEDE-TG-MSS170003 and XSEDE-TG-MSS190008).

Appendix A. Interaction energy between two parallel dislocations

The general form of the interaction energy between two parallel dislocations segments (shown in Fig. A.6) is presented in the classical textbook [26], which can be written as

$$\begin{aligned} W_{12} = & \frac{\mu}{4\pi}\left(\mathbf{b}_1\cdot\boldsymbol{\xi}_1\right)\left(\mathbf{b}_2\cdot\boldsymbol{\xi}_2\right) I\left(x_\alpha, y_\beta\right) \\ & + \frac{\mu}{4\pi(1-\nu)}\left\{\left(\mathbf{b}_1\cdot\mathbf{e}_3\right)\left(\mathbf{b}_2\cdot\mathbf{e}_3\right)\right. \\ & + \left.\left[\left(\mathbf{b}_1\times\boldsymbol{\xi}_1\right)\cdot\mathbf{e}_3\right]\left[\mathbf{e}_3\cdot\left(\mathbf{b}_2\times\boldsymbol{\xi}_2\right)\right]\right\} I\left(x_\alpha, y_\beta\right) \\ & + \frac{\mu}{4\pi(1-\nu)}\left(\mathbf{b}_1\cdot\mathbf{e}_3\right)\left(\mathbf{b}_2\cdot\mathbf{e}_3\right) R\left(x_\alpha, y_\beta\right), \end{aligned} \tag{A.1}$$

where μ is the shear modulus, ν is the Poisson's ratio, $\mathbf{b}$ is the Burgers vector and $\boldsymbol{\xi}$ is the line direction of a dislocation. $\mathbf{e}_2$ points from dislocation 1 to 2, and $\mathbf{e}_3$ is perpendicular to the paper. The term I comes from an integration along the dislocation lines and can be written as

$$I(x,y) = R - (y-x)\ln s - \frac{1}{2}(x-y)\ln t, \tag{A.2}$$

where the distance R is expressed in terms of the local coordinates (x, y) and the distance η

$$\begin{aligned} & R(x,y) = \sqrt{(x-y)^2+\eta^2}, \\ & t = R + x - y, \quad s = R + y - x. \end{aligned} \tag{A.3}$$

Then, Eq. (A.1) can be applied to compute the interaction energy between the parallel dislocations in the periodic system shown in Fig. 2. The interaction energy between the vertical and horizontal dislocations in the primary image can be derived respectively as

$$W_{\mathrm{v}}^0 = -\frac{\mu b^2}{2\pi(1-\upsilon)}\left[s - \left(s^2+h^2\right)^{1/2} + h\ln\frac{h+\left(s^2+h^2\right)^{1/2}}{s}\right], \tag{A.4}$$

and

$$\begin{aligned} W_{\mathrm{h}}^0 = \frac{\mu b^2}{2\pi}\Bigg\{ & \left(s^2+h^2\right)^{1/2} + \left(m^2+h^2\right)^{1/2} - \left[(s+m)^2+h^2\right]^{1/2} \\ & + s\ln\frac{\left[(s+m)^2+h^2\right]^{1/2}+s+m}{\left(s^2+h^2\right)^{1/2}+s} \\ & + m\ln\frac{\left[(s+m)^2+h^2\right]^{1/2}+s+m}{\left(m^2+h^2\right)^{1/2}+m} - s\ln\left(1+\frac{m}{s}\right) - m\ln\left(1+\frac{s}{m}\right)\Bigg\}, \end{aligned} \tag{A.5}$$

where the length parameters s and m are defined Fig. 2, b is the magnitude of Burgers vector and h is the kink height.

The interaction energy between two vertical dislocations from the primary and periodic images can be written as

$$W_{\mathrm{v}}(p,q) = \xi_p\xi_q\frac{\mu b^2}{2\pi(1-\upsilon)}\left[d - \left(d^2+h^2\right)^{1/2} + h\ln\frac{h+\left(d^2+h^2\right)^{1/2}}{d}\right], \tag{A.6}$$

where p and q denote two vertical dislocation segments, and d is the distance between them which can be written in terms of i, L and s. All four terms in Eq. (9) are derived using Eq. (A.6). For $W_{\mathrm{v}}\left(D, D_i\right)$ and $W_{\mathrm{v}}\left(E, E_i\right)$, $\xi_p\xi_q = 1$, indicating the positive interaction energy and repulsive force between two dislocations. For $W_{\mathrm{v}}\left(D, E_i\right)$ and $W_{\mathrm{v}}\left(E, D_i\right)$, $\xi_p\xi_q = -1$, indicating the negative interaction energy and attractive force between two dislocations.

The interaction energy between two horizontal dislocations from the primary and periodic images can be written as

$$W_{\mathrm{h}} = \frac{\mu b^2}{4\pi}\left[I\left(x_1,y_1\right) + I\left(x_2,y_2\right) - I\left(x_1,y_2\right) - I\left(x_2,y_1\right)\right], \tag{A.7}$$

where the term I, defined in Eq. (A.2), is a function of local coordinates. All four terms in Eq. (10) can be written using Eq. (A.7). For the segment pair (A, C_i) and (A, C_i'), $x_1 = 0$, $x_2 = s$, $y_1 = s + i$ and $y_2 = s + iL + m$. For the segment pair (B, C_i) and (B, C_i'), $x_1 = 0$, $x_2 = s$, $y_1 = s + m + (i-1)L$ and $y_2 = s + 2m + (i-1)L$.

Appendix B. First order approximation

In this section, we apply first order approximation to the interactions energies. For dislocation segments in the primary image, their interaction energies written in Eqs. (A.4) and (A.5) can be simplified as

$$W_{\mathrm{v}}^0 = -\frac{\mu b^2 h^2}{4\pi(1-\upsilon)}\frac{1}{s}, \tag{B.1}$$

and

$$W_{\mathrm{h}}^0 = \frac{\mu b^2 h^2}{8\pi}\left(\frac{1}{s}+\frac{1}{m}-\frac{1}{s+m}\right), \tag{B.2}$$

Add them together, the total interaction energy in primary image is:

$$W^0 = -\frac{\mu b^2 h^2}{8\pi}\frac{1+\upsilon}{1-\upsilon}\frac{1}{s} + \frac{\mu b^2 h^2}{8\pi}\left(\frac{1}{m}-\frac{1}{s+m}\right). \tag{B.3}$$

It is noted that when $m \to \infty$, Eq. (B.3) simplifies to:

$$W^0 = -\frac{\mu b^2 h^2}{8\pi s}\frac{1+\nu}{1-\nu}, \tag{B.4}$$

which was introduced in [26] to compute interactions of kink pair on a infinitely long dislocation line, and certainly cannot be applied to the system with periodic boundary conditions.

The interaction energy between primary dislocations and their image i, Eqs. (9) and (10) can be simplified as:

$$W_{\mathrm{h}}^{i} = \frac{\mu b^2 h^2}{8\pi}\left(\frac{1}{iL+s}+\frac{1}{iL-s}-\frac{2}{iL}+\frac{1}{iL+m}+\frac{1}{iL-m} -\frac{1}{iL+s+m}-\frac{1}{iL-s-m}\right), \tag{B.5}$$

and

$$W_{\mathrm{v}}^{i} = -\frac{\mu b^2 h^2}{4\pi(1-\upsilon)}\left(\frac{1}{iL+s}+\frac{1}{iL-s}-\frac{2}{iL}\right). \tag{B.6}$$

Consider the contribution from all periodic images, the total interaction energy can be written in terms of the summation of infinite series:

$$\begin{aligned} W_{\mathrm{int}} &= -\frac{\mu b^2 h^2}{8\pi}\frac{1+\upsilon}{1-\upsilon}\frac{1}{s}+\frac{\mu b^2 h^2}{8\pi}\left(\frac{1}{m}-\frac{1}{s+m}\right) \\ &+ \sum_{i=1}^{\infty}\left[-\frac{\mu b^2 h^2}{8\pi}\frac{1+\upsilon}{1-\upsilon}\left(\frac{1}{iL+s}+\frac{1}{iL-s}-\frac{2}{iL}\right)\right. \\ &+ \left.\frac{\mu b^2 h^2}{8\pi}\left(\frac{1}{iL+m}+\frac{1}{iL-m}-\frac{1}{iL+s+m}-\frac{1}{iL-s-m}\right)\right]. \end{aligned} \tag{B.7}$$

Let $\lambda = s/L$, $\zeta = m/L$ and rearrange Eq. (B.7), we get

$$W_{\mathrm{int}} = -\frac{\mu b^2 h^2}{8\pi L}\frac{1+\upsilon}{1-\upsilon}A+\frac{\mu b^2 h^2}{8\pi L}B, \tag{B.8}$$

where

$$A = \frac{1}{\lambda}+\sum_{i=1}^{\infty}\left(\frac{1}{i+\lambda}+\frac{1}{i-\lambda}-\frac{2}{i}\right), \tag{B.9}$$

and

$$B = \frac{1}{\zeta}-\frac{1}{\lambda+\zeta}+\sum_{i=1}^{\infty}\left(\frac{1}{i+\zeta}+\frac{1}{i-\zeta}-\frac{1}{i+\lambda+\zeta}-\frac{1}{i-\lambda-\zeta}\right). \tag{B.10}$$

In Eq. (B.10), notice that $i+\lambda+\zeta = (i+1)-\zeta$ and $i-\lambda-\zeta = (i-1)+\zeta$. Therefore, all terms in Eq. (B.10) cancel each other, leading to $B = 0$. Finally, Eq. (B.8) is reduced to

$$W_{\mathrm{int}} = -\frac{\mu b^2 h^2}{8\pi L}\frac{1+\upsilon}{1-\upsilon}\left[\frac{1}{\lambda}+\sum_{i=1}^{\infty}\left(\frac{1}{i+\lambda}+\frac{1}{i-\lambda}-\frac{2}{i}\right)\right]. \tag{B.11}$$

References

[1] C.R. Weinberger, B.L. Boyce, C.C. Battaile, Slip planes in bcc transition metals, Int. Mater. Rev. 58 (5) (2013) 296–314.

[2] P. Gordon, T. Neeraj, Y. Li, J. Li, Screw dislocation mobility in BCC metals: the role of the compact core on double-kink nucleation, Modelling Simul. Mater. Sci. Eng. 18 (8) (2010) 085008.

[3] L. Ventelon, F. Willaime, P. Leyronnas, Atomistic simulation of single kinks of screw dislocations in α-Fe, J. Nucl. Mater. 386 (2009) 26–29.

[4] T. Swinburne, S. Dudarev, S. Fitzgerald, M. Gilbert, A. Sutton, Theory and simulation of the diffusion of kinks on dislocations in bcc metals, Phys. Rev. B 87 (6) (2013) 064108.

[5] J. Chaussidon, M. Fivel, D. Rodney, The glide of screw dislocations in bcc Fe: atomistic static and dynamic simulations, Acta Mater. 54 (13) (2006) 3407–3416.

[6] A. Koester, A. Ma, A. Hartmaier, Atomistically informed crystal plasticity model for body-centered cubic iron, Acta Mater. 60 (9) (2012) 3894–3901.

[7] C. Domain, G. Monnet, Simulation of screw dislocation motion in iron by molecular dynamics simulations, Phys. Rev. Lett. 95 (21) (2005) 215506.

[8] M. Gilbert, S. Queyreau, J. Marian, Stress and temperature dependence of screw dislocation mobility in α-Fe by molecular dynamics, Phys. Rev. B 84 (17) (2011) 174103.

[9] N. Zotov, B. Grabowski, Molecular dynamics simulations of screw dislocation mobility in bcc nb, Modelling Simul. Mater. Sci. Eng. 29 (8) (2021) 085007.

[10] S. Narayanan, D.L. McDowell, T. Zhu, Crystal plasticity model for BCC iron atomistically informed by kinetics of correlated kinkpair nucleation on screw dislocation, J. Mech. Phys. Solids 65 (2014) 54–68.

[11] L. Proville, D. Rodney, M.-C. Marinica, Quantum effect on thermally activated glide of dislocations, Nature Mater. 11 (10) (2012) 845–849.

[12] N. Zotov, B. Grabowski, Entropy of kink pair formation on screw dislocations: an accelerated molecular dynamics study, Modelling Simul. Mater. Sci. Eng. 30 (6) (2022) 065004.

[13] F. Maresca, D. Dragoni, G. Csányi, N. Marzari, W.A. Curtin, Screw dislocation structure and mobility in body centered cubic Fe predicted by a Gaussian approximation potential, Npj Comput. Mater. 4 (1) (2018) 1–7.

[14] L. Dezerald, L. Proville, L. Ventelon, F. Willaime, D. Rodney, First-principles prediction of kink-pair activation enthalpy on screw dislocations in bcc transition metals: V, Nb, Ta, Mo, W, and Fe, Phys. Rev. B 91 (9) (2015) 094105.

[15] R.K. Barik, A. Ghosh, D. Chakrabarti, Fundamental insights on ductile to brittle transition phenomenon in ferritic steel, Materialia (2022) 101667.

[16] R. Ji, T. Phan, H. Chen, L. Xiong, Quantifying the dynamics of dislocation kinks in iron and tungsten through atomistic simulations, Int. J. Plast. 128 (2020) 102675.

[17] G. Hachet, D. Caillard, L. Ventelon, E. Clouet, Mobility of screw dislocation in BCC tungsten at high temperature in presence of carbon, Acta Mater. 222 (2022) 117440.

[18] D. Rodney, L. Proville, Stress-dependent peierls potential: Influence on kink-pair activation, Phys. Rev. B 79 (9) (2009) 094108.

[19] A. Stukowski, D. Cereceda, T.D. Swinburne, J. Marian, Thermally-activated non-schmid glide of screw dislocations in W using atomistically-informed kinetic Monte Carlo simulations, Int. J. Plast. 65 (2015) 108–130.

[20] P. Hirel, Atomsk: A tool for manipulating and converting atomic data files, Comput. Phys. Comm. 197 (2015) 212–219.

[21] A.P. Thompson, H.M. Aktulga, R. Berger, D.S. Bolintineanu, W.M. Brown, P.S. Crozier, P.J. in 't Veld, A. Kohlmeyer, S.G. Moore, T.D. Nguyen, R. Shan, M.J. Stevens, J. Tranchida, C. Trott, S.J. Plimpton, LAMMPS - a flexible simulation tool for particle-based materials modeling at the atomic, meso, and continuum scales, Comput. Phys. Comm. 271 (2022) 108171.

[22] G. Henkelman, B.P. Uberuaga, H. Jónsson, A climbing image nudged elastic band method for finding saddle points and minimum energy paths, J. Chem. Phys. 113 (22) (2000) 9901–9904.

[23] D. Sheppard, P. Xiao, W. Chemelewski, D.D. Johnson, G. Henkelman, A generalized solid-state nudged elastic band method, J. Chem. Phys. (ISSN: 00219606) 136 (7) (2012) http://dx.doi.org/10.1063/1.3684549.

[24] A. Ghasemi, P. Xiao, W. Gao, Nudged elastic band method for solid-solid transition under finite deformation, J. Chem. Phys. (ISSN: 00219606) 151 (5) (2019) http://dx.doi.org/10.1063/1.5113716.

[25] A. Stukowski, Visualization and analysis of atomistic simulation data with OVITO–the open visualization tool, Modelling Simul. Mater. Sci. Eng. 18 (1) (2009) 015012.

[26] P.M. Anderson, J.P. Hirth, J. Lothe, Theory of Dislocations, Cambridge University Press, 2017.

[27] M.-C. Marinica, L. Ventelon, M. Gilbert, L. Proville, S. Dudarev, J. Marian, G. Bencteux, F. Willaime, Interatomic potentials for modelling radiation defects and dislocations in tungsten, J. Phys.: Condens. Matter 25 (39) (2013) 395502.

[28] D. Caillard, Kinetics of dislocations in pure Fe. Part I. In situ straining experiments at room temperature, Acta Mater. 58 (9) (2010) 3493–3503.

[29] D. Caillard, An in situ study of hardening and softening of iron by carbon interstitials, Acta Mater. 59 (12) (2011) 4974–4989.

[30] D. Caillard, Geometry and kinetics of glide of screw dislocations in tungsten between 95K and 573K, Acta Mater. 161 (2018) 21–34.

[31] U.F. Kocks, A. AS, A. MF, Thermodynamics and kinetics of slip, 1975.